International Journal of Heat and Mass Transfer 52 (2009) 1123–1131

Contents lists available at ScienceDirect

International Journal of Heat and Mass Transfer

journal homepage: www.elsevier.com/locate/ijhmt

Pore migration under high temperature and stress gradients

Simon P.A. Gill *

Department of Engineering, University of Leicester, University Road, Leicester LE1 7RH, UK

ARTICLE INFO

Article history:
Received 2 October 2007
Available online 19 November 2008

Keywords:
Porous media
Pore migration
Heat transport
Surface diffusion
Crack growth
Uranium dioxide

ABSTRACT

An analytical model is proposed for the evolution of ellipsoidal pores by surface diffusion under the influence of large temperature gradients and the associated thermoelastic stress field. It is found that both of these influences affect the migration velocity of a pore as well as its shape. The shape of a pore is determined by competition between the thermoelastic stress field, the interfacial energies of the pore and grain boundaries, and the kinetics of the mass transport process. The dramatic case of void migration in a uranium dioxide nuclear fuel rod is considered, in which very large temperature gradients of the order of 4×10^5 K/m are predicted. It is found that crack-like pores are expected to form on the radial grain boundaries prevalent in the fuel rod microstructure, and that these crack-like pores lead to the eventual structural failure of the component. This agrees with experimental observations. The temperature gradient is the dominant driving force for the migration of near-spheroidal and prolate pores, whereas the stress field is the dominant driving force for oblate crack-like pores.

1. Introduction

Heat transport through porous media has been the subject of much attention [1–3]. In the majority of studies it is assumed that the pores are of a fixed size, shape and position within the medium. In this paper, however, an analysis of heat and mass transport in a temperature gradient by the translational movement and morphological change of pores is presented. The medium of interest is uranium dioxide, from which fuel rods used in nuclear power reactors are manufactured. Large amounts of heat are generated within these rods during fission. The centre of the rod experiences high temperatures (up to 2000 K) with much lower temperatures at the outside of the rod. The low thermal conductivity of uranium dioxide leads to the development of very large temperature gradients (up to 4×10^5 K/m [4]) which provide a strong driving force for the migration of pores. Large stresses are also generated within the fuel rods due to this non-uniform temperature distribution and these can also play a role in the rearrangement of material [5]. Initially the cylindrical fuel pellets have a uniform, equiaxed, fine-grained microstructure with randomly distributed pores of about 1 μm in radius [6]. The formation of gaseous products during services can also lead to the development of sub-micron pores. A cross-section of a midservice uranium dioxide fuel rod is shown in Fig. 1 [6]. Tikare and Holm [6] identified five regions in this microstructure. Region 1 is a very large central void running the length of the rod, which is assumed to be due to the coalescence of pores which have migrated up the thermal gradient towards the centre of the rod. Taking the radius of the rod to be R, this central void is approximately defined if the radial distance from the centre, r, satisfies $r < 0.3R$. Region 2 ($0.3R < r < 0.7R$) consists of a highly columnar grain structure in which the grain boundaries are predominantly radial in nature. Lenticular pores are observed at the ends of the columnar grains, as shown in the inset in Fig. 1. It is also evident in this region that there are a large number of radial cracks which have propagated though the sample. Some have propagated all the way through the fuel rod and some only extend a lesser distance from the central void, indicating that this is the site of their initiation. These cracks will be discussed further in the light of predictions about the migration of pores in Section 4. Region 3 ($0.7R < r < 0.85R$) contains enlarged equiaxed grains with a uniform distribution of pores, indicating some grain growth but little net pore migration. The microstructure in region 4 ($0.85R < r < R$) is similar to the initial pre-service microstructure, indicating that the temperatures in this region were not sufficient for evolution to occur. The outer region 5 represents the steel cladding placed around the fuel rod. This is preserving the overall structural integrity of the rod given the level of cracking observed. It is the aim of this paper to explain these observations so that microstructures can be optimised to avoid these high levels of voidage and cracking.

In this paper, a model for pore migration based on a novel variational formulism [7] is constructed in Section 2. This assumes that the pore migrates and changes shape by surface diffusion. There are a number of simultaneous driving forces for these processes, namely the temperature gradient, the associated thermoelastic stress field, and the free surface energy of the pore and the interfacial energy attributed to the grain boundaries. The

Tel.: +44 116 252 5055; fax: +44 116 252 2525.
E-mail address: spg3@le.ac.uk.

0017-9310/$ - see front matter © 2008 Elsevier Ltd. All rights reserved.
doi:10.1016/j.ijheatmasstransfer.2008.10.004

Nomenclature

a_0	the radius of a spherical pore of an equivalent volume
α	shape parameter for ellipsoidal pore, defined by Eq. (1)
m	shape parameter for ellipsoidal pore, defined by Eq. (21)
∇T	remote temperature gradient
$\nabla \hat{T}$	locally enhanced temperature gradient
σ_{xx}, σ_{yy}, σ_{zz}	principal thermoelastic stresses
σ_r, σ_θ, σ_z	principal thermoelastic stresses in cylindrical coordinates
Π	variational functional
Ψ	dissipation potential for kinetic processes
$\dot{G}$	rate of change of Gibb's free energy
j	volumetric surface flux
A_s	surface area of the pore
D_s	surface diffusivity
V	pore velocity
$C_{\alpha\alpha}$, C_{VV}	dissipation rate coefficients
Q^*	heat of transport
F_T	driving force per unit volume due to temperature gradient
β	shape factor for local temperature gradient enhancement
I_1	Eshelby coefficient
γ	interfacial energy densities
I	shape functions for Gibbs free energy dependence
K	shape functions for rate of change of Gibbs free energy dependence
η	ratio of grain boundary energy to pore free surface energy
σ_0	reference stress
R	reference length (taken to be fuel pellet radius)
E	elastic Youngs' modulus of UO_2
α_T	thermal expansion coefficient of UO_2
ν	Poissons' ratio of UO_2
λ	dimensionless material groups defined by Eq. (14)
$\bar{r}$	radial distance normalised with respect to reference length
$\bar{\sigma}$	stress normalised with respect to reference stress
V_{sphere}	velocity of a spherical pore
k	stress ratio
T	temperature
k_T	thermal conductivity of UO_2
$\dot{q}$	rate of heat generation in UO_2 fuel rod per unit volume

Subscripts

T	corresponding to thermal gradients
S	corresponding to pore free surface interface
B	corresponding to grain boundary interfaces
E	corresponding to elastic strain

evolution of a typical uranium dioxide fuel rod microstructure is considered in Section 3 and discussed in Section 4 in the context of the in-service observations made above.

2. The pore migration model

The three-dimensional pores are assumed to have an ellipsoidal shape, as shown in Fig. 2. The volume of the pore is assumed to remain constant and its surface is defined in terms of spherical polar coordinates

$$\begin{aligned} x &= a_0 \alpha \cos\theta \cos\phi \\ y &= a_0 \alpha \cos\theta \sin\phi \quad \text{for } 0 \leq \alpha < \infty \\ z &= a_0 \alpha^{-2} \sin\theta \end{aligned} \tag{1}$$

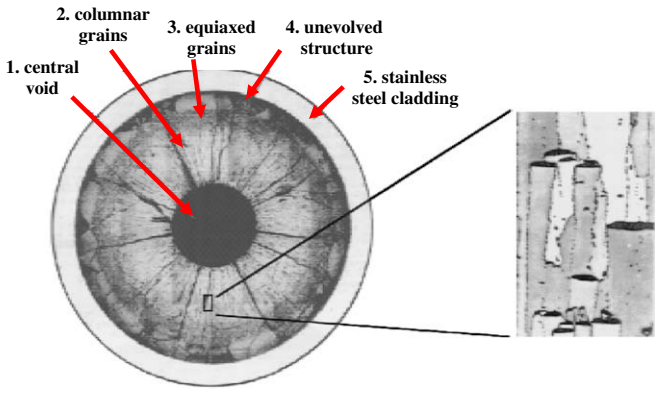

Fig. 1. Micrograph of the midservice microstructure in a UO_2 fuel. There is a very large void at the centre of the pellet due to the migration of pores to this region. Five circular banded regions of different material behaviour have been identified. The inset shows the columnar microstructure that has developed in region 2. Reproduced with permission of Blackwell Publishing, [6] V. Tikare, E.A., Holm, Simulation of grain growth and pore migration in a thermal gradient, J. Am. Ceram. Soc. 81 (1998) 480-484. Copyright [1998] American Ceramic Society.

where $-\pi \leqslant \varphi \leqslant \pi$, $-\pi/2 \leqslant \theta \leqslant \pi/2$, α is a shape parameter and a_0 is the radius of a spherical pore of an equivalent volume. The pore has rotational symmetry about the z-axis and is described as oblate if $\alpha > 1$ and prolate if $\alpha < 1$. The pore shape can therefore range from a rod-like prolate crack ($\alpha = 0$) to a sphere ($\alpha = 1$) to a penny-shaped crack ($\alpha = \infty$). Some useful geometric properties of ellipsoids are summarised in Appendix A. The pore is assumed to move with a net velocity V in the x-direction due to a constant temperature gradient ∇T and to gradients in the consequent thermoelastic stress field. The major axes of the ellipsoids are assumed to be subjected to a principal stress state such that there are no shear stresses, the normal stress along the z-axis is σ_{zz} and the normal stresses in the (x,y) plane, $\sigma_{xx} = \sigma_{yy}$, are equal.

The evolution of such a pore is now elaborated within the context of a variational framework [7]. This integral method has the advantage that the exact evolutionary morphology of the system does not need to be known. The pore is assumed to evolve within the class of ellipsoidal morphologies. If the system evolves within this class of morphologies then the exact solution to the problem is obtained. If it is not, then the best approximation to the exact result within the constraints of this class is found. In general we formulate a variational functional

$$\Pi = \Psi + \dot{G} \tag{2}$$

such that the actual kinematic field describing the evolution is the minimal one, i.e. $\delta\Pi = 0$. We assume that the pore evolves via diffusion of atoms over its surface. The kinetics of the surface diffusion process are encapsulated within the dissipation potential, Ψ. The rate of change of Gibb's free energy, $\dot{G}$, provides the driving force for this mechanism, where the dot indicates differentiation with respect to time. Assuming the surface diffusivity is isotropic, the dissipation potential can be written as

$$\Psi = \frac{1}{2} \int_{A_s} \frac{j^2}{D_s} dS \tag{3}$$

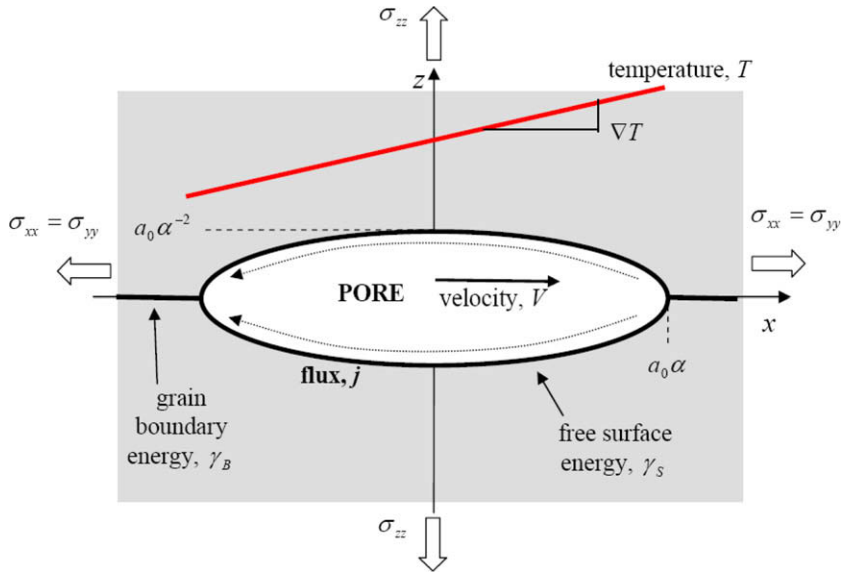

Fig. 2. The ellipsoidal pore has its major axes orientated along the x, y and z-directions. The x and y-directions are assumed to be equivalent except for the fact that the pore is assumed to move with a velocity V in the x-direction under the action of a temperature gradient ∇T and a stress field defined by $\sigma_{xx} = \sigma_{yy}$ and σ_{zz}. The parameter a_0 defines the volume of the pore and the shape parameter, α, defines the eccentricity of the ellipsoid. The pore is assumed to be placed on a grain boundary in the $z = 0$ plane. The shape of the pore is determined by the stress field, the free surface energy of the pore, the energy of the grain boundary and the mass transport kinetics. Material is assumed to rearrange via surface diffusion at a rate determined by the material flux, j.

where j is the volumetric surface flux, A_s is the surface area of the pore, and D_s is the surface diffusivity, which is assumed to be constant over the dimensions of the pore. The pore can evolve to either change its shape ($\dot{\alpha} \neq 0$) or position ($V \neq 0$) over time. The dissipation potential Eq. (3) can therefore be expressed in terms of the two degrees-of-freedom as

$$\Psi = \frac{2\pi a_0^4}{D_s \alpha^5}\left(C_{\alpha\alpha} a_0^2 \dot{\alpha}^2 + C_{VV} V^2\right) \tag{4}$$

where the matrix components $C_{\alpha\alpha}(\alpha)$ and $C_{VV}(\alpha)$, defined by (B13), are simply functions of the pore shape. As shown in Appendix B, there is no interaction between shape change and the translational motion of the pore.

The driving force term can be written as the sum of three contributions

$$\dot{G} = \dot{\Phi}_T + \dot{G}_S + \dot{G}_E \tag{5}$$

due to the temperature gradient (T), the interfacial energies (S) and the elastic strain energy (E). The driving force due to the thermal gradient is not due to a change in Gibbs free energy, as it is usually associated with a change in the enthalpy of the system [8]. However, this is analogous to an electromigration force [9] and hence can be treated as such. The force acting on a unit volume of material in a local temperature gradient $\nabla \hat{T}$ is given by Nichols [10]

$$F_T = -Q^* \frac{\nabla \hat{T}}{T} \tag{6}$$

where T is the absolute temperature and Q^* is known as the heat of transport. This is defined as the thermal energy released by a unit volume of material as it moves down a temperature gradient [11]. This flow of heat in the x-direction is therefore associated with a flux of material j_x in the same direction, and hence the total driving force is

$$\dot{\Phi}_T = \int_{A_s} F_T j_x dS \tag{7}$$

Assuming that F_T is constant over the dimensions of the pore, it is observed that it provides no net driving force for changing the shape of the pore. The only non-zero contribution is therefore from the translational motion of the pore and, using Eq. (C2),

$$\dot{\Phi}_T = -\frac{4\pi}{3}\beta Q^* \frac{\nabla T}{2T} a_0^3 V \tag{8}$$

where the remote temperature gradient ∇T is locally enhanced by the pore such that the local temperature gradient $\nabla \hat{T} = \beta \nabla T$ where $\beta(\alpha) > 1$ is a dimensionless function of the pore shape given by Carslaw and Jaegar [12] to be

$$\beta(\alpha) = \frac{4\pi}{4\pi - I_1(\alpha)} \tag{9}$$

where $I_1(\alpha)$ is an Eshelby coefficient, defined by Eq. (C3). The value of β ranges from 2 to 1.5 to 1 as α goes from 0 to 1 to ∞.

The driving forces for shape change are interfacial energy and elastic strain energy. It has been observed in Fig. 1 that the grain boundary orientation is predominantly radial in region 2, the region where significant pore migration is occurring. Hence, assuming that the pore is symmetrically oriented along a radial grain boundary in the $z = 0$ plane, as shown in Fig. 2, the total interfacial energy is given by

$$G_S = 4\pi\alpha_0^2\left[\gamma_S I_S(\alpha) - \frac{1}{4}\gamma_B \alpha^2\right] \tag{10}$$

where γ_S and γ_B are the interfacial energy densities of the free surface of the pore and grain boundaries, respectively, and $I_S(\alpha)$ is the shape function defined by Eq. (C5). The driving force due to the interfacial energy is therefore

$$\dot{G}_S = 4\pi a_0^2 \gamma_s [K_S - \eta\alpha]\dot{\alpha} \tag{11}$$

where $\eta = \frac{\gamma_B}{2\gamma_S}$ and $K_S = \frac{dI_S}{d\alpha}$. Physically it is expected that $0 < \eta < 1$. If $\eta > 1$ then the interfacial energy will drive a pore to become crack-like in the initial pre-service microstructure which is not observed.

The thermoelastic stress field induced by a temperature gradient also generates gradients in the global stress field. It is assumed here that the remote stress field local to the pore is approximately uniform, given the small change in the stresses within the dimensions of the pore. However, as the pore moves through the body it

will experience the changes in the global stress field associated with the large changes in its position (relative to its own dimensions). In this case the elastic strain energy in the body can change due to a change in the pores shape and its position. The expression for the strain energy is elaborated in Appendix C. Its time derivative is given by

$$\dot{G}_E = -\frac{4\pi a_0^3 \sigma_0^2}{3E}\left(K_E^{\alpha}\dot{\alpha} + K_E^{V}\frac{V}{R}\right) \tag{12}$$

where σ_0 is a reference stress, R is a reference length, E is the Youngs' modulus of the material, and the coefficients K_E^{α} and K_E^{V} depend on the pore shape and the solution for the global thermoelastic stress field.

The variational functional Eq. (1) is now completely defined by (4) and (12). The stationary solution occurs when

$$\begin{aligned}\frac{d\alpha}{dt} &= \frac{\alpha^5}{C_{\alpha\alpha}(\alpha)}\left(K_E^{\alpha}(\alpha,\bar{r}) - \lambda_S[K_S(\alpha) - \eta\alpha]\right)\\ \frac{d\bar{r}}{dt} &= \bar{a}_0^2\frac{\alpha^5}{C_{VV}(\alpha)}\left(K_E^{V}(\alpha,\bar{r}) + \lambda_T\beta(\alpha)\frac{1}{T}\frac{dT}{d\bar{r}}\right)\end{aligned} \tag{13}$$

where the following dimensionless material parameters have been introduced

$$\lambda_S = \frac{3E\gamma_S}{a_0\sigma_0^2} \quad \lambda_T = \frac{EQ^*}{2\sigma_0^2} \tag{14}$$

Dimensionless time is related to real time by $\bar{t} = \left(\frac{D_s\sigma_0^2}{3Ea_0^3}\right)t$ and $\bar{r} = r/R$ is the non-dimensionalised position of the pore etc. The two rate equations are coupled through their interdependence on the current shape and position of the pore.

From Eq. (13) it can be seen that the velocity of a spherical pore in the absence of thermoelastic effects is

$$V_{sphere} = \frac{15D_sQ^*}{4a_0T}\frac{dT}{dr} \tag{15}$$

which predicts that a pore will move up a temperature gradient if $Q^* > 0$ and that a small pore will migrate faster than a large one. Note that Q^* is the heat of transport for uranium dioxide complexes here. It is not to be confused with the heat of transport of oxygen interstitials in uranium dioxide, which is known to be negative [13].

The stability of a spherical pore moving through a homogeneous medium ($\eta = 0$) to perturbations in its shape is governed by $K_E^{\alpha}(1,\bar{r}) - \lambda_S K_S(1)$. Now $K_S(1) = 0$ so it is expected that a pore will be spherical if $K_E^{\alpha}(1,\bar{r}) = 0$, become prolate if $K_E^{\alpha}(1,\bar{r}) < 0$ and oblate if $K_E^{\alpha}(1,\bar{r}) > 0$. Assuming $\sigma_{zz} \neq 0$, we can write this using Eqs. (C8) and (C9) as

$$(594 - 630\nu) - (306 - 630\nu)k - 288k^2 = 0 \tag{16}$$

where $k = \frac{\sigma_{xx}}{\sigma_{zz}}$. This has solutions $k_1 = 1$ and $k_2 = \frac{(35\nu-33)}{16} = -1.41$ for $\nu = 0.3$ [14]. Hence a void is expected to be a sphere if k has one of these values, an oblate spheroid if $k_2 < k < 1$ and a prolate spheroid if $1 < k < k_2$. To make further progress it is necessary to consider the exact nature of the global temperature field and consequent thermoelastic field that the pore resides within. This is the subject of the next section.

3. The evolution of a pore in a uranium dioxide nuclear fuel rod

Pore migration in uranium dioxide nuclear fuel pellets has been reported as an extreme problem, leading to the eventual structural failure of the pellet [6]. This is due to the strong temperature gradients that arise because of the low thermal conductivity of uranium dioxide. The thermal conditions in such pellets have recently been simulated by Ramirez et al. [4]. They consider a cylindrical pellet of uranium dioxide of radius $R = 4.3$ mm which is placed within a steel cladding of thickness 0.5 mm. There is a small argon-filled gap between the cladding and the pellet. It is predicted [4,15] that the temperature in the centre of this relatively small pellet during operation is approximately 1150 K, reducing to about 750 K at the perimeter. The steady-state axisymmetric temperature distribution satisfies

$$\frac{1}{r}\frac{d}{dr}(rk_TT) = -\dot{q} \tag{17}$$

where k_T is the thermal conductivity and $\dot{q}$ is the rate of heat generation per unit volume. For a comparable, simple analytic solution, we assume that both of these quantities are constant, and then the steady-state temperature profile is simply

$$T(r) = \frac{1}{4}A(R^2 - r^2) + 750 \tag{18}$$

where the value of $A \approx 10^8$ K/m^2 equates to a thermal conductivity of $k_T = 2$W/K m for the assumed heat generation rate of $\dot{q} = 2\times10^8$ W/m^3 [4]. This agrees well with results of Ramirez et al. (see Fig. 3 in [4]) and gives a zero temperature gradient at the centre of the pellet and a maximum temperature gradient of -2×10^5 K/m at the perimeter. This is a conservative estimate compared to the values of -4×10^5 K/m quoted by Ramirez et al. [4] and -5.4×10^6 K/m by Michels and Poeppel [16] that arise in pellets of larger radius. The associated thermoelastic field in cylindrical coordinates (r,θ,Z) is easily determined from Lamés equations [17] for a pellet subjected to no external loading

$$\begin{aligned}\sigma_r &= \frac{A\alpha_TE}{16}(r^2 - R^2)\\ \sigma_\theta &= \frac{A\alpha_TE}{16}(3r^2 - R^2)\\ \sigma_Z &= \nu\frac{A\alpha_TE}{16}(4r^2 - 2R^2)\end{aligned} \tag{19}$$

where α_T is the thermal expansion coefficient of UO_2 and plane strain conditions have been assumed. Close inspection of these terms shows that, for a typical Poisson ratio of $\nu = 0.3$ [14], the radial and longitudinal stress components are similar. Given that it is the stress differences that play an important role, and that the steel cladding could play an undetermined role in defining the thermoelastic boundary conditions, it is assumed here that the stress state can be approximated by letting $\sigma_Z = \sigma_r$. The z-axis of an oblate spheroid is expected to align along the direction of maximum ten-

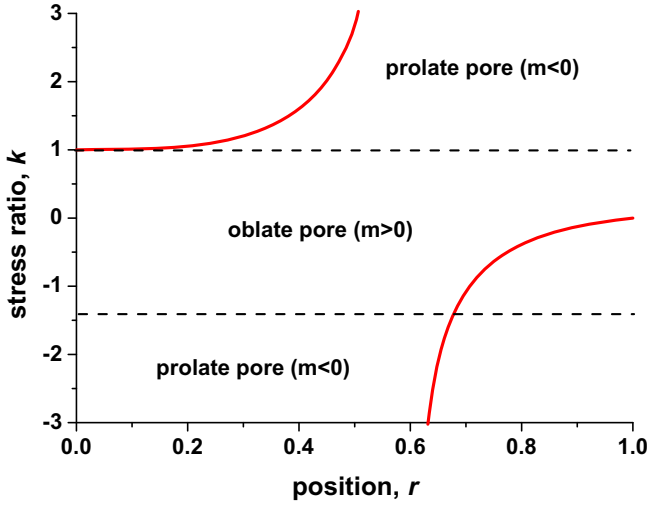

Fig. 3. The stress ratio, $k = \frac{\sigma_{xx}}{\sigma_{zz}}$, varies with radial position, $\bar{r}$, through the cylindrical uranium dioxide fuel pellet. The equilibrium shape of a pore in a homogenous solid is expected to be prolate ($\alpha < 1$) for $k > 1$ and $k < -1.41$ and oblate ($\alpha > 1$) for $-1.41 < k < 1$ and spheroidal ($\alpha = 1$) on the boundaries.

sile stress (σ_θ) [18] so at the microscale of the pore we associate the hoop direction (θ) with the z-axis in Fig. 2. The temperature gradient is in the radial direction (r) which is therefore associated with the direction of motion of the pore, along the x-axis in Fig. 2. The y-axis is identical to the x-axis in terms of the shape, and this is therefore associated with the z-axis in cylindrical coordinates. The stress state can therefore be expressed in dimensionless terms as simply

$$\bar{\sigma}_{xx} = \bar{\sigma}_{yy} = (\bar{r}^2 - 1)$$
$$\bar{\sigma}_{zz} = (3\bar{r}^2 - 1) \tag{20}$$

where the radial distance and stresses have been written in a dimensionless form, $\bar{r} = \frac{r}{R}$ and $\bar{\sigma}_{xx} = \frac{\sigma_{xx}}{\sigma_0}$ etc., where the reference stress has been taken to be $\sigma_0 = \frac{R^2 A \alpha_T E}{16}$. The stresses in the x and y-directions are always negative (compressive) whereas the stress in the z-direction changes from compressive at the centre to tensile on the outside at $\bar{r} = 0.58$. There is therefore a middle band of low stress centered around $\bar{r} = 0.58$ with a high compressive stress region at the centre and a high, predominantly tensile, stress region at the perimeter. Fig. 3 shows the variation in the stress ratio, $k = \frac{\sigma_{xx}}{\sigma_{zz}}$, though the pellet along with the equilibrium pore shape classification predicted by (16). The critical radius at which a transition from prolate to oblate pores occurs at $\bar{r} = \sqrt{\frac{k_2 - 1}{3k_2 - 1}} = 0.68$. The exact equilibrium pore shape is now explored.

3.1. Equilibrium pore shape

Taking the reference length to be the pellet radius, $R = 4.3$ mm, and using the material properties $E = 2 \times 10^{11}$ N/m^2 [14] and $\alpha_T = 10^{-5}$ K^{-1} [19] for uranium dioxide and a typical pore radius of $a_0 = 10^{-6}$ m [6], we have a reference stress of $\sigma_0 = 200$ MPa. The surface energy density is estimated to be $\gamma_s = 0.3$ J/m^2 [19] which predicts that $\lambda_S = 4.5$ for a 1 μm pore. To explore the range of shapes that a pore can adopt we introduce the shape parameter [18]

$$m = \frac{\alpha^2 - 1}{\alpha^2 + 1} \tag{21}$$

where $-1 \leqslant m \leqslant 1$ as $0 \leqslant \alpha \leqslant \infty$. The extreme cases are for a sphere ($m = 0$), an oblate plate-like crack ($m = 1$) and a prolate rod-like crack ($m = -1$). The equilibrium pore shape is given by the value of α that satisfies $\frac{d\alpha}{dt} = 0$ in Eq. (13a). This is plotted in Fig. 4 as a function of the pores radial position in the pellet. Fig. 4a shows the effect of the grain boundary/surface energy ratio, η, on the equilibrium pore shape. Firstly, for a pore in a homogenous solid ($\eta = 0$), one finds that the pore is fairly equiaxed for pores at the centre of the pellet ($\bar{r} < 0.68$) where prolate pores are preferred. This is because the elastic strain energy reduction is not a strong function of shape for prolate spheroids. However, for the region where oblate spheroids are predicted ($\bar{r} > 0.68$), the pores are expected to undergo a very rapid transition into a crack-like morphology as oblate cracks release large amounts of strain energy. The effect of placing the pore on a grain boundary ($\eta > 0$) shows that the pore can further reduce its interfacial energy by becoming more oblate. For high-energy grain boundaries ($\eta > 0.3$) one finds that this can drive pores at the centre of the pellet to become crack-like as well as pores at the perimeter. This is a graver problem, as these pores evolve quickly due to the higher temperature at the centre, whereas the pores at the lower temperature perimeter are not commonly observed to evolve significantly (see Fig. 1). There is a region centred around $\bar{r} = 0.58$ where pores are not predicted to become crack-like under any circumstances as the stress levels in this region are too low.

Note that the value of the dimensionless parameter, $\lambda_S = \frac{3E\gamma_S}{a_0\sigma_0^2}$, is expected to be subject to some variation. The surface energy and the pore size could easily vary by a factor of 2 either way,

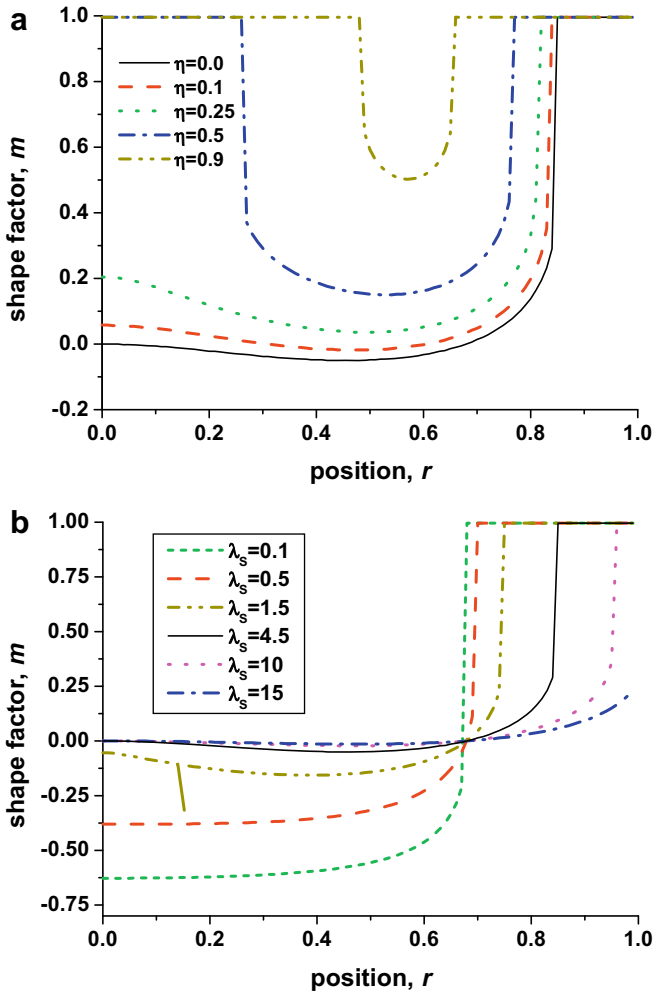

Fig. 4. Equilibrium pore shape, m, (21) as a function of radial position, $\bar{r}$, in the uranium dioxide fuel pellet for (a) varying grain boundary energy, η, and (b) varying pore size, λ_S. The high tensile stresses at the perimeter of the pellet favour crack-like ($m = 1$) pores, although these are only suppressed if λ_S dominates. Radial high-energy grain boundaries (large η) make it favourable for crack-like pores to form near the centre of the pellet.

and the reference stress could easily be increased by an order of magnitude if larger pellets were considered. Therefore there is significant possible variation in the value of this parameter. Fig. 4b illustrates the effect of this parameter on the expected equilibrium pore shape. Low values of $\lambda_S < 1$ mean that the strain energy dominates the equilibrium morphology of the pore in accordance with Fig. 3. Highly prolate pores are favoured towards the centre of the pellet and there is a sharp transition to crack-like oblate pores near the periphery with few equiaxed pores predicted at all. At high values of $\lambda_S > 10$ the interfacial energy dominates and suppresses the formation of crack-like pores in favour of near-spheroidal ones. This distinction is important. It suggests that, for a given situation, small pores are more stable and likely to remain equiaxed. Large pores may evolve more slowly but they are more likely to evolve into dangerous crack-like features.

3.2. Kinetics of pore migration and shape change

The equilibrium shape of pores was considered in the previous subsection. However, a pore may not attain its equilibrium shape as its behaviour is governed by its kinetics as well as its thermodynamics. In this subsection the kinetics of pore migration and shape

change are considered by solving the combined system of equations (13). The kinetics are strongly dependent on the heat of transport parameter, Q^*. The density of UO_2 is 10,970 kg/m^3 and it weighs 0.270 kg/mol so, using previous parameters, we can write $\lambda_T = 100Q^*$ where Q^* is given in kJ/mol. The exact value of the heat of transport of uranium dioxide is not known but data on the heat of transport of oxygen in uranium dioxide suggests that it will be very sensitive to the exact stoichiometry of the compound at a particular position [4]. Therefore it is not possible to estimate its value although it is expected to be in the range of $0 < Q^* < 100$ kJ/mol. Negative values are not expected given that pores are observed to migrate up a temperature gradient to the centre of a pellet. It is found that pores have time to adopt their equilibrium shape if the migrational driving force (effectively determined by the magnitude of Q^*) is small compared to the forces driving shape change. For a high migration force of $Q^* = 100$ kJ/mol the pore does not necessarily reach its equilibrium morphology. However, for $Q^* < 10$ kJ/mol pores evolve very close to their equilibrium shape. Some pore trajectories are shown in Fig. 5 for four different cases where the pore does not have sufficient time to reach its equilibrium shape everywhere. Initially nine spheroidal pores are placed at positions $\bar{r} = n/10$ where $n = 1, \ldots, 9$ on the $m = 0$ axis. The evolution of the pores shape and position are shown. The equilibrium predictions of Fig. 4 are also shown as dotted lines for comparison. The first three cases illustrate the expected response for the best-guess case of $\lambda_S = 4.5$ and $Q^* = 100$ kJ/mol. Fig. 5a illustrates pore evolution in a homogeneous pellet ($\eta = 0$). All the pores move towards the centre of the pellet ($\bar{r} = 0$). The pore at $\bar{r} = 0.9$ does not attain its equilibrium shape of an oblate crack. It migrates towards the centre of the pellet whilst it is elongating and reaches a position in the pellet where its equilibrium shape is that of a near-spheroid before it becomes crack-like. It is then stable and proceeds along the same equilibrium trajectory as the other pores. Note that time proceeds non-linearly along the trajectories. This is partly because the pore velocity depends on the pore shape, but principally because the temperature increases towards the centre of the pellet so surface diffusion is very much faster there. The case in Fig. 5a therefore predicts that pores will remain approximately spheroidal in the absence of grain boundaries and will move with a velocity approximately given by Eq. (15). Pores on radial grain boundaries,

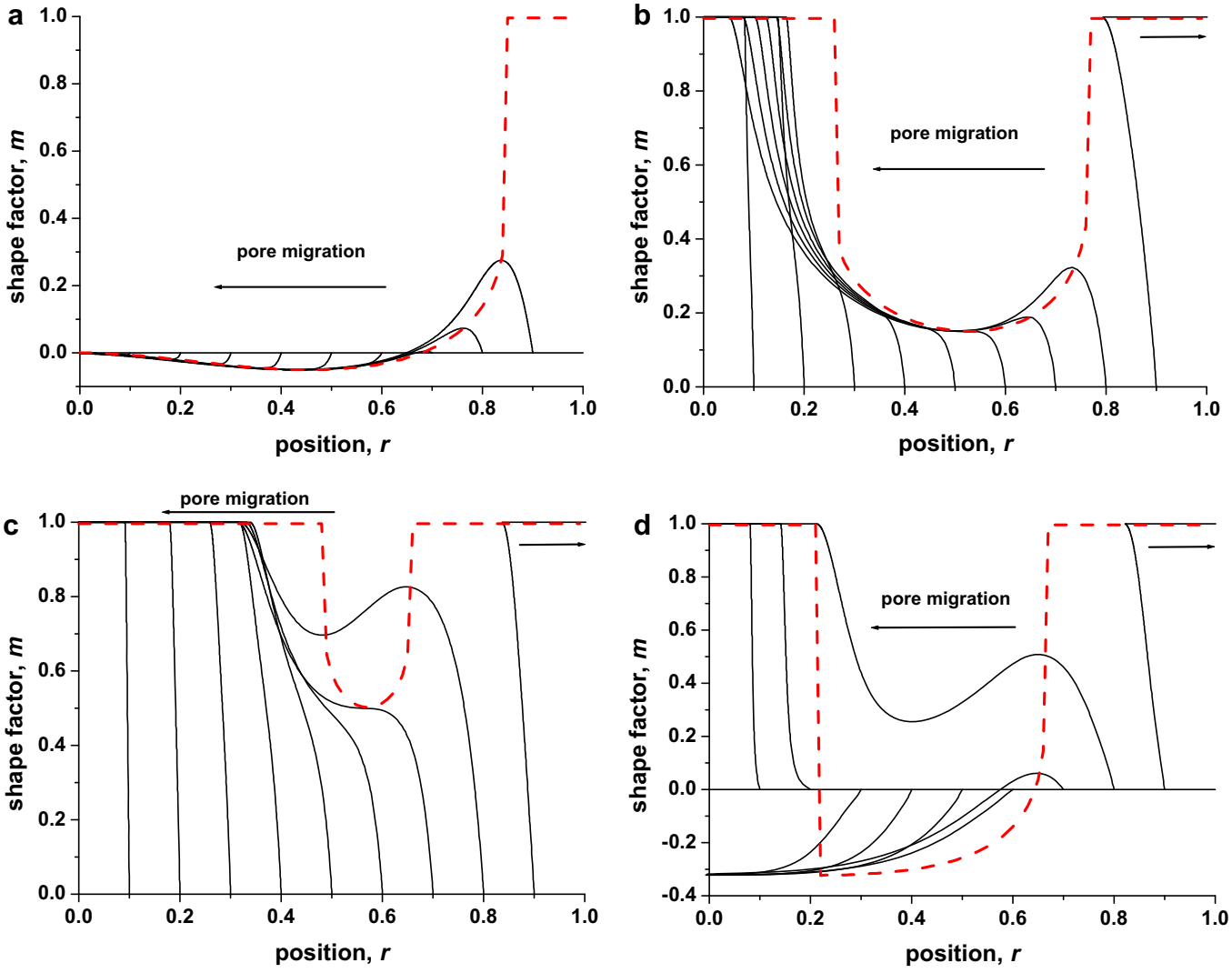

Fig. 5. Pore trajectories for different material parameters for $\lambda_S = 4.5$ and (a) homogeneous medium ($\eta = 0$), (b) low-energy grain boundary ($\eta = 0.5$), (c) high-energy grain boundary ($\eta = 0.9$) and (d) for $\lambda_S = 0.5$ with $\eta = 0.5$. Nine spheroidal pores are initially place at $\bar{r} = 0.1, 0.2, \ldots, 0.9$ on the $m = 0$ axis. These are allowed to evolve according to (13). The equilibrium pore shapes are a function of position are shown as a red dotted line. The expected heat of transport $Q^* = 100$ kJ/mol provides a strong migratory driving force such that some pores do not attain their equilibrium shape. The thermal gradient driving force dominates the migration of prolate and near-spheroidal pores and drives them to the centre of the pellet. The driving force due to the thermoelastic stress field dominates for crack-like pores ($m = 1$). This drives crack-like pores towards the centre for $\bar{r} < 0.58$ and towards the perimeter for $\bar{r} > 0.58$.

however, will not in general remain spheroidal as shown in Fig. 5b and c. For the case of a low-energy grain boundary ($\eta = 0.5$), shown in Fig. 5b, the majority of pores get close to their equilibrium shape as the move through the pellet towards the centre. However, the sharp transition from a near-spheroidal pore to an oblate crack-like pore at $\bar{r} = 0.25$ is smoothed out due to the kinetics of the shape change process. The pore starting at $\bar{r} = 0.9$ initially is of interest as it moves inwards as its shape evolves to become more crack-like but then changes direction and moves outwards towards the edge of the pellet once it reaches a crack-like morphology. This indicates a change in the mechanism for migration of this pore. In general the thermal gradient driving force overwhelmingly dominates the thermoelastic driving force for near-spheroidal pores if $Q^* > 0.1$ kJ/mol as expected. The variation in velocity with shape for prolate or near-spheroidal pores ($\alpha < 2$, say) is not greatly significant, especially compared to the large change in the surface diffusivity with temperature through the pellet. However, this is not the case for high-aspect ratio oblate pores. In the limit of large α, using the limiting expressions in Appendix B and Appendix C in (13), one finds that the translational velocity of a pore can be approximated by

$$\begin{aligned}\frac{d\alpha}{d\bar{t}} &= 12\left(\frac{6}{\pi}(1-\nu^2)\bar{\sigma}_{zz}^2\alpha - \lambda_S(1-\eta)\right)\alpha^3 \\ \frac{d\bar{r}}{d\bar{t}} &= 16\bar{a}_0^2\left(\frac{4}{\pi}(1-\nu^2)\bar{\sigma}_{zz}\frac{d\bar{\sigma}_{zz}}{d\bar{r}}\alpha^3 + \lambda_T\frac{1}{T}\frac{dT}{d\bar{r}}\right)\alpha^2\end{aligned} \tag{22}$$

where the first term on the right hand side is the driving force to the thermoelastic field and the second is that due to the thermal gradient. Firstly one notes that the velocity and rate of shape change increase very rapidly as α^5 and α^4, respectively, as the oblate pore becomes more crack-like. Secondly, the elastic driving force rapidly increases with α but the thermal driving force does not. Therefore there will be some critical value for the pore shape for which the thermoelastic effects dominate the thermal effects. For the temperature field considered in this paper, the extremes in the stress field occur at the centre ($\bar{r} = 0$) and perimeter ($\bar{r} = 1$) of the pellet. At these points one finds that the two driving forces are of approximately equal magnitude when $\alpha \approx 0.5\lambda_T^{1/3}$. This occurs when $\alpha = 2.5$ when $Q^* = 1$ kJ/mol, $\alpha = 5$ when $Q^* = 10$ kJ/mol and $\alpha = 10$ when $Q^* = 100$ kJ/mol. Hence the thermoelastic effect is significant for oblate pores with aspect ratios of this order and above. Note that the thermal field always acts to drive pores to the centre. The elastic field acts to drive pores towards the centre only for $\bar{r} < 0.58$ and it drives pores out of the pellet towards the perimeter when $\bar{r} > 0.58$. This is the explanation for the observations for the $\bar{r} = 0.9$ pore in Fig. 5b. It moves towards the centre of the pellet whilst it is fairly round under the influence of the thermal gradient driving force but, as its shape evolves towards a crack, the thermoelastic driving force begins to dominate and the pore changes direction to move to the perimeter of the pellet. Although the evolution of this pore is probably only of academic interest, as it is unlikely to evolve in the low temperature perimeter region, the other crack-like pores (at the centre of the pellet) will evolve rapidly and the dominant thermoelastic driving force will accelerate their migration to the centre of the pellet. If the crack-like pores are weakly developed then this may result in their subsequent coalescence into the large central void and therefore render them less hazardous for further crack propagation. However, if the pores have developed into extensive crack-like features by this time they could be unstable. The ratio of crack propagation rate, $a_0\dot{\alpha}$, to pore migration rate, $\dot{r}$, for large α is given by (22) to be $\frac{a_0\dot{\alpha}}{\dot{r}} = \frac{9\bar{\sigma}_{zz}}{8\bar{a}_0\alpha}\left(\frac{d\bar{\sigma}_{zz}}{d\bar{r}}\right)^{-1}$. For a pore on the edge of the central void ($\bar{r} = 0.3$) this predicts that $\frac{a_0\dot{\alpha}}{\dot{r}} \approx \frac{1}{\bar{a}_0\alpha}$. Although α is large, this ratio will be greater than one (as $\alpha > \bar{a}_0$ corresponds to a crack that exceeds the dimensions of the pellet). Therefore it is highly possible that crack-like pores exist for which the crack propagation rate will exceed the migration rate. These crack-like pores will continue to progress through the body until they reach a critical length whereby fast fracture occurs. Fig. 5c shows that high-energy grain boundaries ($\eta = 0.9$) increase the possibility of this scenario. This case is of particular interest as the pore starting at $\bar{r} = 0.8$ initially becomes elongated, then contracts as it moves into a lower stress region, and then elongates again as it enters the central high-stress region. The example in Fig. 5d illustrates some of the other phenomena that can be observed. This is for a large pore on a low-energy grain boundary under a strong thermal gradient driving force. The pores in the middle band ($0.3 < \bar{r} < 0.7$) move towards their equilibrium prolate shape. Upon reaching the central region $\bar{r} < 0.2$ they would be driven to become more crack-like if they were spheroidal (as in the case of the pores starting as $\bar{r} = 0.1$ and 0.2). However, as they are prolate at that point they see another local energy minima and move towards an increasingly prolate shape rather than an oblate one. As in Fig. 5c, the pore at $\bar{r} = 0.8$ experiences a temporary shape change reversal as it proceeds through the low stress region.

4. Conclusions

The picture of pore migration constructed in Section 3 is consistent with the microstructural observations of Section 1 and Fig. 1 [6]. The basic picture is that pores migrate up the temperature gradient into the centre of the rod and coalesce to form a large void along the length of the rod. This was previously understood and recognised. However, the evolution of the pore shape, the effect of the thermoelastic field and the interactions between pores and grain boundaries have not been previously considered. These all add more detail to the picture. Firstly, it seems likely from the formation of a columnar microstructure in region 2 of Fig. 1, that a large number of pores within the evolving medium interact with grain boundaries. If the grain boundaries lie normal to the migration path of the pores, then the pores can get trapped on the grain boundaries. The migration force causes the pores to drag these grain boundaries along with them. They may eventually escape the grain boundary but a succession of pores migrating past will continue to cause the elongation of the grains. This results in the formation of lenticular pores at the end of long radial grains. These grain boundaries reduce the mobility of pores and hence are of less interest than boundaries tangential to the direction of pore migration. They are, however, of significance as they produce large numbers of these highly-orientated radial boundaries. The behaviour of pores situated on these radial boundaries has been considered in this paper. They are important because they are the only favourable sites within the pore migration region (region 2) for the evolution of near-spheroidal pores into penny-shaped crack-like features. This anisotropy in pore shape is favoured as it reduces the area/energy of the grain boundary interface and because it is an effective shape for allowing the thermoelastic stress field to do work. Crack-like pores on radial grain boundaries are also highly mobile. The driving forces on these pores due to the thermal gradient and the thermoelastic stress field both act in the same direction and are of comparable magnitudes. Small pores are less likely to become elongated and crack-like than larger pores. However, it is predicted that small pores will coalesce into large pores during the migration process [6]. It is predicted that large crack-like pores have time to form on high-energy grain boundaries in region 2 before they are predicted to coalesce with the central void of region 1. In this case it is expected that a large number of radial crack-like features will emanate from the central void. This is observed in Fig. 1, where a number of these crack-like features have been found to be of sufficient length to initiate fast fracture.

In summary, a model has been proposed for the evolution of ellipsoidal pores by surface diffusion in a nuclear fuel rod under the influence of large temperature gradients and the associated thermoelastic

stress field. Both of these influences affect the migration velocity of a pore, as well as its shape. The shape of the pore is determined by competition between the stress field, the interfacial energies of the pore and grain boundaries, and the mass transport kinetics. It is found that crack-like pores are expected to be observed on radial grain boundaries for the estimated material parameters. It is predicted that these crack-like pores lead to the eventual structural failure of the component. The temperature gradient is the dominant driving force for the migration of near-spheroidal pores, whereas the stress field is the dominant driving force for crack-like pores.

Appendix A. Geometrical quantities for ellipsoids

Given a position on the surface, $\underline{x}$, from (1), the two orthogonal tangent vectors to the pore surface are given by

$$\begin{aligned}\underline{s}_\theta &= \frac{\partial \underline{x}}{\partial \theta} = a_0\alpha[-\sin\theta\cos\phi, -\sin\theta\sin\phi, \alpha^{-3}\cos\theta]\\ \underline{s}_\phi &= \frac{\partial \underline{x}}{\partial \phi} = a_0\alpha[-\cos\theta\sin\phi, \cos\theta\cos\phi, 0]\end{aligned} \tag{A1}$$

which are directed along the φ = constant and θ = constant lines, respectively. They have magnitudes

$$\begin{aligned}|\underline{s}_\theta| &= a_0\alpha^{-2}\sqrt{\cos^2\theta + \alpha^6\sin^2\theta}\\ |\underline{s}_\phi| &= a_0\alpha\cos\theta\end{aligned} \tag{A2}$$

The unit outward normal to the surface is given by

$$\underline{n} = \frac{(\underline{s}_\theta \times \underline{s}_\phi)}{|\underline{s}_\theta \times \underline{s}_\phi|} = \frac{[\cos\theta\cos\phi, \cos\theta\sin\phi, \alpha^3\sin\theta]}{\sqrt{\cos^2\theta + \alpha^6\sin^2\theta}} \tag{A3}$$

where $|\underline{s}_\theta \times \underline{s}_\phi| = |\underline{s}_\theta||\underline{s}_\phi|$ for orthogonal vectors. The area of a surface element is

$$dS = |\underline{s}_\theta \times \underline{s}_\phi| d\theta d\phi = a_0^2\alpha^{-1}\cos\theta\sqrt{\cos^2\theta + \alpha^6\sin^2\theta}\, d\theta d\phi \tag{A4}$$

Flux is constrained to the x–z plane for translation of the pore. The unit tangent and outward normal to the surface in this plane are therefore

$$\underline{t}_y = \frac{[-\alpha^3\sin\theta, 0, \cos\theta\cos\phi]}{\sqrt{\cos^2\theta\cos^2\phi + \alpha^6\sin^2\theta}} \quad \underline{n}_y = \frac{[\cos\theta\cos\phi, 0, -\alpha^3\sin\theta]}{\sqrt{\cos^2\theta\cos^2\phi + \alpha^6\sin^2\theta}} \tag{A5}$$

Appendix B. The dissipation potential

The two components of the surface flux field in spherical polars, j_θ and j_φ, are orientated along the φ = constant and θ = constant lines, respectively. They can be expressed as

$$\begin{aligned}j_\theta &= j_\theta^\alpha + j_\theta^V\\ j_\phi &= j_\phi^\alpha + j_\phi^V\end{aligned} \tag{B1}$$

where the superscripts indicate fluxes associated with either shape change (α) or translation (V). By considering the flux into and out of a surface element, the surface flux is related to the normal velocity of the surface v_n by

$$v_n = -\frac{1}{|\underline{s}_\theta||\underline{s}_\phi|}\left(\frac{\partial(|\underline{s}_\phi| j_\theta)}{\partial\theta} + \frac{\partial(|\underline{s}_\theta| j_\phi)}{\partial\phi}\right) \tag{B2}$$

where the lengths $|\underline{s}_\theta|$ and $|\underline{s}_\phi|$ are given in Appendix A. The inward normal velocity of the pore surface has components due to shape change and translation so

$$v_n = v_n^\alpha + v_n^V \tag{B3}$$

where

$$v_n^\alpha = -\dot{\underline{x}}.\underline{n} = -a_0\dot{\alpha}\frac{(\cos^2\theta - 2\sin^2\theta)}{\sqrt{\cos^2\theta + \alpha^6\sin^2\theta}} \tag{B4}$$

using (1) and Eq. (A3), and

$$v_n^V = -[V, 0, 0].\underline{n} = -\frac{V\cos\theta\cos\phi}{\sqrt{\cos^2\theta + \alpha^6\sin^2\theta}} \tag{B5}$$

For shape change, the flux field is symmetric about the z-axis so $j_\phi^\alpha = 0$. In this case Eq. (B2) can be rearranged to give

$$j_\theta^\alpha(\theta,\phi) = -\frac{1}{|\underline{s}_\phi|}\int_0^\theta |\underline{s}_\theta||\underline{s}_\phi| v_n d\theta = \frac{a_0^2\dot{\alpha}}{2\alpha^2}\sin 2\theta \tag{B6}$$

For translational motion, the flux field is confined to the x–z plane and hence the non-zero flux component is written as $j_{xz}^V(\theta,\phi)$. This can be written in terms of the spherical polar components as

$$\begin{aligned}j_\theta^V &= j_{xz}^V \underline{t}_y \cdot \frac{\underline{s}_\theta}{|\underline{s}_\theta|} = j_{xz}^V\cos\phi\sqrt{\frac{\cos^2\theta + \alpha^6\sin^2\theta}{\cos^2\theta\cos^2\phi + \alpha^6\sin^2\theta}}\\ j_\phi^V &= j_{xz}^V \underline{t}_y \cdot \frac{\underline{s}_\phi}{|\underline{s}_\phi|} = j_{xz}^V\frac{\alpha^3\sin\theta\sin\phi}{\sqrt{\cos^2\theta\cos^2\phi + \alpha^6\sin^2\theta}}\end{aligned} \tag{B7}$$

The fluxes can therefore be related to the motion of the surface by writing Eq. (B2) in the form

$$v_n = -\frac{1}{|\underline{s}_\theta||\underline{s}_\phi|}\left(\frac{\partial(f\cos\theta\cos\phi)}{\partial\theta} + \frac{\partial(f\sin\theta\sin\phi)}{\partial\phi}\right) \tag{B8}$$

where the variable $f = a_0\alpha\sqrt{\frac{\cos^2\theta+\alpha^6\sin^2\theta}{\cos^2\theta\cos^2\phi+\alpha^6\sin^2\theta}} j_{xz}^V$ has been introduced. When constrained to this y = constant plane, the angles are related by $dy = 0$ such that $d\varphi = \tan\theta\tan\varphi\, d\theta$ from (1). The above can therefore be simplified to give

$$f = -\int_0^\theta \frac{v_n|\underline{s}_\theta||\underline{s}_\phi|}{2\cos\theta\cos\phi}d\theta = \frac{a_0^2 V}{2\alpha}\sin\theta \tag{B9}$$

One can therefore write

$$j_{xz}^V(\theta,\phi) = \frac{a_0 V}{2\alpha^2}\sin\theta\sqrt{\frac{\cos^2\theta\cos^2\phi + \alpha^6\sin^2\theta}{\cos^2\theta + \alpha^6\sin^2\theta}} \tag{B10}$$

The dissipation potential (3) can now be written as

$$\begin{aligned}\Psi &= \frac{1}{2}\int_{A_s}\frac{j^2}{D_s}dS = \frac{1}{2D_s}\int_{A_s}\left(j_\theta^2 + j_\phi^2\right)dS\\ &= \frac{1}{2D_s}\int_{A_s}\left[(j_\theta^\alpha)^2 + 2j_\theta^\alpha j_\theta^V + (j_{xz})^2\right]dS\end{aligned} \tag{B11}$$

which can be expressed in the form

$$\Psi = \frac{2\pi a_0^4}{D_s\alpha^5}[\,a_0\dot{\alpha} \quad V\,]\begin{bmatrix}C_{\alpha\alpha} & C_{\alpha V}\\ C_{\alpha V} & C_{VV}\end{bmatrix}[\,a_0\dot{\alpha}\,] \tag{B12}$$

where

$$\begin{aligned}C_{\alpha\alpha} &= \frac{\alpha^5}{4\pi a_0^6\dot{\alpha}^2}\int_{A_s}(j_\theta^\alpha)^2 dS = \int_0^{\frac{\pi}{2}}\sin^2\theta\cos^3\theta\sqrt{\cos^2\theta + \alpha^6\sin^2\theta}\,d\theta\\ C_{\alpha V} &= \frac{\alpha^5}{4\pi a_0^5\dot{\alpha}V}\int_{A_s} j_\theta^\alpha j_\theta^V dS = 0\\ C_{VV} &= \frac{\alpha^5}{4\pi a_0^4 V^2}\int_{A_s}(j_{xz}^V)^2 dS = \frac{1}{8}\int_0^{\frac{\pi}{2}}\sin^2\theta\cos\theta\frac{(\cos^2\theta + 2\alpha^6\sin^2\theta)}{\sqrt{\cos^2\theta + \alpha^6\sin^2\theta}}d\theta\end{aligned} \tag{B13}$$

The result $C_{\alpha V} = 0$ indicates that there is no dissipative interaction between shape change and translational movement. The non-zero coefficients $C_{\alpha\alpha}$ and C_{VV} have analytical expressions but are too unwieldy to be reproduced here. They are easier calculated numerically but the following limiting values are useful:

$C_{\alpha\alpha}(0) = \pi/32$, $C_{vv}(0) = \pi/128$ $C_{\alpha\alpha}(1) = 2/15$, $C_{vv}(1) = 1/15$, and in the limit of $\alpha \to \infty$ one finds that $C_{\alpha\alpha}(\infty) \to 1/12\,\alpha^3$ and $C_{vv}(\infty) \to 1/16\,\alpha^3$.

Appendix C. Driving forces

The flux in the x-direction is given by

$$j_x = \left[j^V_{xz} \underline{t}_y + j^{\alpha}_{\theta} \frac{\underline{S}_{\theta}}{|\underline{S}_{\theta}|} \right] \cdot [1,0,0] \tag{C1}$$

where the variables are defined by Eqs. (A1), (A2), (A5), (B6), and (B10). The non-zero contribution to the total flux over the surface (due to j^V_{xz}) is therefore

$$\int_{A_s} j_x dS = \frac{2\pi a_0^3}{3} V \tag{C2}$$

The Eshelby coefficient used in the calculation of β (9) is given for an oblate spheroid by Mura [20]

$$I_1(\alpha) = \begin{cases} \frac{2\pi}{(\alpha^6-1)^{\frac{3}{2}}} \left[\alpha^6 \cos^{-1}(\alpha^{-3}) - \sqrt{\alpha^6 - 1} \right] & \text{if } \alpha > 1 \\ \frac{4\pi}{3} & \text{if } \alpha = 1 \\ \frac{2\pi}{(1-\alpha^6)^{\frac{3}{2}}} \left[\sqrt{1-\alpha^6} - \alpha^6 \cosh^{-1}(\alpha^{-3}) \right] & \text{if } \alpha < 1 \end{cases} \tag{C3}$$

For a constant surface energy density γ_S, the surface energy of a pore is given by

$$G_S = \int_{A_s} \gamma_s dS = 4\pi a_0^2 \gamma_s I_S(\alpha) \tag{C4}$$

where, from (A4),

$$I_S(\alpha) = \begin{cases} \frac{\alpha^2}{2} + \frac{\ln(\sqrt{\alpha^6-1}+\alpha^3)}{2\alpha\sqrt{\alpha^6-1}} & \text{if } \alpha > 1 \\ 1 & \text{if } \alpha = 1 \\ \frac{\alpha^2}{2} + \frac{1}{8\alpha\sqrt{1-\alpha^6}} \left[\pi - 2\tan^{-1}\left(\frac{2\alpha^6-1}{2\alpha^3\sqrt{1-\alpha^6}} \right) \right] & \text{if } \alpha < 1 \end{cases} \tag{C5}$$

The elastic strain energy of an isotropically elastic body containing an ellipsoidal inclusion subject to a uniform remote stress field has been calculated by Eshelby [21] and summarised by Mura [20]. Sun et al. [18] have written the solution for the reduced case of an oblate spheroid subjected to the principal stresses $\sigma_{xx} = \sigma_{yy}$ and σ_{zz}. If we assume that the local stress state over the dimensions of the pore is unaffected by any gradients in the stress field, the change in energy due to the introduction of the pore is

$$G_E = -\frac{4\pi a_0^3}{3E} \left(\sigma_{xx}^2 C_{11} + \sigma_{xx}\sigma_{zz}(C_{13} + \frac{1}{2}C_{31}) + \frac{1}{2}\sigma_{zz}^2 C_{33} \right) \tag{C6}$$

where E is the Youngs' modulus of the material, and the dimensionless coefficients C_{ij} are functions of the Poisson ratio v and the pore shape α and are given in Appendix A of Sun et al. [18]. Useful limiting expressions for the elastic shape coefficients are $C_{11} = \frac{12(1-v)}{(7-5v)}$, $C_{13} = \frac{1}{2}C_{31} = -\frac{3(1+5v)(1-v)}{2(7-5v)}$ and $C_{33} = \frac{3(9+5v)(1-v)}{2(7-5v)}$ for a spheroid ($\alpha = 1$). For an oblate crack-like spheroid ($\alpha \to \infty$) the coefficients are all of order one except for $C_{33} \to \frac{4}{\pi}(1-v^2)\alpha^3$ which dominates. For a prolate crack-like spheroid ($\alpha = 0$) the coefficients are simply $C_{11} = 2, C_{13} = \frac{1}{2}C_{31} = -v$ and $C_{33} = 1$.

Globally we expect the stress field to be a function of the pores position in the body, r, and hence the rate of change of the elastic strain energy depends on both the translational velocity and rate of shape change of the pore such that

$$\dot{G}_E = -\frac{4\pi a_0^3 \sigma_0^2}{3E} \left(K^{\alpha}_E \dot{\alpha} + K^V_E \frac{V}{R} \right) \tag{C7}$$

where σ_0 is a reference stress, $\overline{\sigma}_{xx} = \sigma_{xx}/\sigma_0$, $\overline{r} = r/R$, where R is a reference length and the dimensionless coefficients are

$$\begin{aligned} K^{\alpha}_E &= \overline{\sigma}_{xx}^2 \frac{dC_{11}}{d\alpha} + \overline{\sigma}_{xx}\overline{\sigma}_{zz} \left(\frac{dC_{13}}{d\alpha} + 1/2 \frac{dC_{31}}{d\alpha} \right) + 1/2\overline{\sigma}_{zz}^2 \frac{dC_{33}}{d\alpha} \\ K^V_E &= [2C_{11}\overline{\sigma}_{xx} + (C_{13} + 1/2C_{31})\overline{\sigma}_{zz}] \frac{d\overline{\sigma}_{xx}}{d\overline{r}} \\ &\quad + [(C_{13} + 1/2C_{31})\overline{\sigma}_{xx} + C_{33}\overline{\sigma}_{zz}] \frac{d\overline{\sigma}_{zz}}{d\overline{r}} \end{aligned} \tag{C8}$$

To determine the stability of a spherical void it is useful to know that

$$\begin{aligned} &\frac{dC_{11}}{d\alpha} = -288D \quad \frac{dC_{13}}{d\alpha} = \frac{1}{2}\frac{dC_{31}}{d\alpha} = (153 - 315v)D \\ &\frac{dC_{33}}{d\alpha} = 4(297 - 315v)D \end{aligned} \tag{C9}$$

for $\alpha = 1$, where $D = \frac{(1-v^2)}{343-490v+175v^2}$.

References

[1] Wu-Shung Fu, Hsin-Chien Huang, Effects of a random porosity model on heat transfer performance of porous media, Int. J. Heat Mass Transfer 42 (1999) 13–25.
[2] O.G. Martynenko, N.V. Pavlyukevich, O.S. Rabinovich, M. Kaviany, Principles of heat transfer in porous media, Int. J. Heat Mass Transfer 36 (1993) 1715–1716.
[3] M. Inoue, K. Abe, I. Sato, A method for determining an effective porosity correction factor for thermal conductivity in fast reactor uranium–plutonium oxide fuel pellets, J. Nucl. Mater. 281 (2000) 117–128.
[4] J.C. Ramirez, M. Stan, P. Cristea, Simulations of heat and oxygen diffusion in UO_2 nuclear fuel rods, J. Nucl. Mater. 359 (2006) 174–184.
[5] Yu.I. Dimitrienko, Thermal stresses and heat-mass transfer in ablating composite materials, Int. J. Heat Mass Transfer 38 (1995) 139–146.
[6] V. Tikare, E.A. Holm, Simulation of grain growth and pore migration in a thermal gradient, J. Am. Ceram. Soc. 81 (1998) 480–484.
[7] A.C.F. Cocks, S.P.A. Gill, J. Pan, Modelling of microstructural evolution, Adv. Appl. Mech. 36 (1999) 81–162.
[8] P.G. Shewmon, Diffusion in Solids, J. Williams, Jenks, OK, 1983. pp. 231–239.
[9] L. Xia, A.F. Bower, Z. Sou, C.F. Shih, A finite element analysis of the motion and evolution of voids due to strain and electromigration-induced surface diffusion, J. Mech. Phys. Solids 45 (1997) 1473–1493.
[10] F.A. Nichols, Kinetics of diffusional motion of pores in solids, J. Nucl. Mater. 30 (1969) 143–165.
[11] K.G. Denbigh, The thermodynamics of the steady state, in: Methuen Monograph on Chemical Subjects, Wiley, 1951, pp. 54–64.
[12] H.S. Carslaw, J.C. Jaeger, Conduction of Heat in Solids, Clarendon Press, Oxford, 1973. pp. 176–178.
[13] C. Sari, G. Schumacher, Oxygen redistribution in fast reactor oxide fuel, J. Nucl. Mater. 61 (1976) 192–202.
[14] R.G. Munro, Elastic Moduli Data for Polycrystalline Ceramics, in NISTIR 6853. National Institute of Standards and Technology, Gaithersburg, Maryland 20899, 2002.
[15] A.C. Rapier, T.M. Jones, J.E. Mclintosh, The thermal conductance of uranium dioxide/stainless steel interfaces, Int. J. Heat Mass Transfer 6 (1963) 397–416.
[16] L.C. Michels, R.B. Poeppel, In-pile migration of fission product inclusions in mixed-oxide fuels, J. Appl. Phys. 44 (1973) 1003–1008.
[17] S.P. Timoshenko, J.N. Goodier, Theory of Elasticity, third ed., McGraw-Hill, New York, 1970. pp. 136–140.
[18] B. Sun, Z. Suo, A.G. Evans, Emergence of cracks by mass transport in elastic crystals stressed at high temperatures, J. Mech. Phys. Solids 42 (1994) 1653–1677.
[19] J.M. Fink, Thermophysical properties of uranium dioxide, J. Nucl. Mater. 279 (2000) 1–18.
[20] T. Mura, Micromechanics of Defects in Solids, second ed., Martinus Nijhoff, Dordrecht, 1987. pp. 74–85.
[21] J.D. Eshelby, The determination of the elastic field of an ellipsoidal inclusion and related problems, Proc. R. Soc. A 241 (1957) 376–396.